Article

High-strength Damascus steel by additive manufacturing

https://doi.org/10.1038/s41586-020-2409-3

Received: 14 November 2019

Accepted: 27 March 2020

Published online: 24 June 2020

Check for updates

Philipp Kürnsteiner[1]✉, Markus Benjamin Wilms[2], Andreas Weisheit[2], Baptiste Gault[1,3], Eric Aimé Jägle[1,4] & Dierk Raabe[1]

Laser additive manufacturing is attractive for the production of complex, three-dimensional parts from metallic powder using a computer-aided design model[1–3]. The approach enables the digital control of the processing parameters and thus the resulting alloy's microstructure, for example, by using high cooling rates and cyclic re-heating[4–10]. We recently showed that this cyclic re-heating, the so-called intrinsic heat treatment, can trigger nickel-aluminium precipitation in an iron–nickel–aluminium alloy in situ during laser additive manufacturing[9]. Here we report a Fe19Ni5Ti (weight per cent) steel tailor-designed for laser additive manufacturing. This steel is hardened in situ by nickel-titanium nanoprecipitation, and martensite is also formed in situ, starting at a readily accessible temperature of 200 degrees Celsius. Local control of both the nanoprecipitation and the martensitic transformation during the fabrication leads to complex microstructure hierarchies across multiple length scales, from approximately 100-micrometre-thick layers down to nanoscale precipitates. Inspired by ancient Damascus steels[11–14]—which have hard and soft layers, originally introduced via the folding and forging techniques of skilled blacksmiths—we produced a material consisting of alternating soft and hard layers. Our material has a tensile strength of 1,300 megapascals and 10 per cent elongation, showing superior mechanical properties to those of ancient Damascus steel[12]. The principles of in situ precipitation strengthening and local microstructure control used here can be applied to a wide range of precipitation-hardened alloys and different additive manufacturing processes.

Parts built by laser additive manufacturing (LAM) experience a specific thermal history. First comes a rapid quenching from the liquid state, followed by an intrinsic heat treatment (IHT), that is, cyclic re-heating that consists of a multitude of short temperature spikes[6,9,15]. In directed energy deposition (DED), parts are built layer-wise by laser melting of powder fed by a carrier gas through a nozzle[1,3]. In DED, the IHT is pronounced and hence provides opportunities to locally adjust the microstructures[7–9,15,16]. Yet new materials must be tailor-designed to best exploit these specific conditions, as conventional alloy compositions cannot be expected to perform efficiently as they have been optimized for other processing routes, for example, casting or forging.

We recently showed that the IHT can trigger nickel-aluminium (NiAl) precipitation in an iron–nickel–aluminium (Fe–Ni–Al) alloy[9]. This so-called maraging steel draws properties from two important phase transformations. Initially, a soft nickel-rich martensitic microstructure forms upon quenching through an austenite-to-martensite transformation. This martensite is later hardened by a second phase transformation to form intermetallic nanoprecipitates. Therefore, conventionally produced as well as LAM-produced commercial maraging steels (for example, 18Ni-300) need to undergo a costly ageing treatment to form property-enhancing intermetallic precipitates[17–22]. Iron–nickel–titanium (Fe–Ni–Ti) alloy systems show extremely fast kinetics for Ni_3Ti precipitation[17–19,21–23], making them ideally suited for in situ precipitation hardening by exploiting the short temperature peaks during IHT.

Here the digital control of the DED process parameters allowed us to locally exploit these two phase transformations and adjust the microstructure to create a new material inspired by Damascus steel. The layered structure of Damascus steel originally resulted from repeatedly folding and forging macrocomposites consisting of a hard steel and a soft steel and lends excellent strength and ductility to the composite[11–14]. We utilize this concept here and produce a Damascus-like maraging steel, not by folding and forging but by fabricating layered microstructures by exploiting rapid quenching, sequential in situ heating and local phase transformation. We specifically designed an Fe19Ni5Ti (wt%) alloy to exploit the rapid quenching and IHT of the DED (see Methods section Supplementary discussion of the alloy design concept' for more details). We adjusted the DED process parameters to regulate the time–temperature profile during the fabrication process, which enabled precise, local control of the martensite formation as well as the

[1]Department Microstructure Physics and Alloy Design, Max-Planck-Institut für Eisenforschung, Düsseldorf, Germany. [2]Fraunhofer Institute for Laser Technology ILT, Aachen, Germany. [3]Department of Materials, Royal School of Mines, Imperial College London, London, UK. [4]Present address: Institute of Materials Science, Universität der Bundeswehr München, Neubiberg, Germany. ✉e-mail: p.kuernsteiner@mpie.de

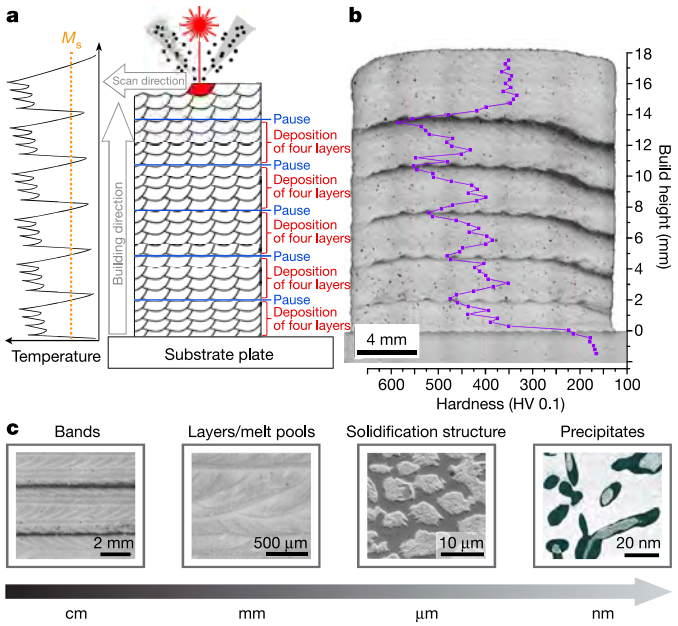

Fig. 1 | DED-produced Fe19Ni5Ti (wt%) sample. a, A schematic of the DED process including a simple sketch of the temperature profile that also shows the martensite start temperature M_s. After building four layers in a sequence, the process was paused for 120 s, allowing the sample to cool. **b**, A light optical micrograph showing a dark band at the position where a pause was introduced. The overlay of the hardness curve shows a peak in hardness at each dark band. **c**, An overview of the hierarchy of the microstructural features at different length scales that are discussed throughout this paper.

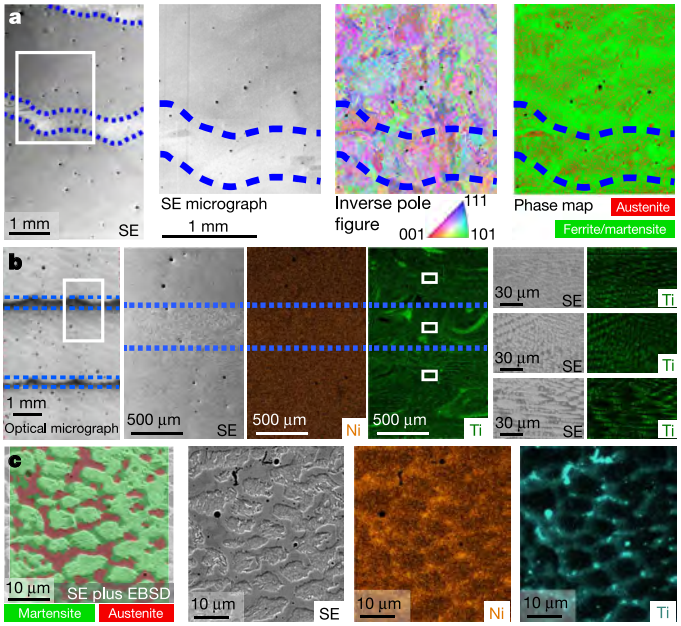

Fig. 2 | Microstructure characterization at different length scales. The hard regions/bands are marked by dashed blue lines. These hard regions appear dark in the optical micrographs because of the rough surface that scatters light away. However, this rougher surface emits a higher number of secondary electrons (SEs), which lets the hard bands appear bright in the electron micrographs. The white boxes mark the area that is magnified in the images to the right. **a**, An SE micrograph featuring two hard regions and the corresponding EBSD maps across one hard band. The inverse pole figure map is in the sample build direction. **b**, Two hard regions in an optical micrograph plus elemental mapping of Ni and Ti at different magnifications. **c**, An SE micrograph with an EBSD map overlaid and the corresponding elemental mapping of Ni and Ti at higher magnification than **b**. Inhomogeneities in the Ti distribution result from the mixing of Ti powder particles due to Marangoni convection as well microsegregation that results in austenite stabilization at interdendritic regions.

precipitation, and hence of the mechanical behaviour. Our approach avoids a time-consuming and costly post-process ageing heat treatment, and also provides the possibility to locally tune the microstructure, which would not be possible with conventional heat treatments.

Results and discussion

Overview

We built a cuboidal part with Fe19Ni5Ti (wt%) maraging steel by DED. DED, as a LAM approach, uses a computer-controlled deposition strategy that, here, included a 120-s pause after a block of four layers. During this pause, the laser was switched off and the sample cooled. A schematic of the process and a micrograph are shown in Fig. 1. The pause led to the formation of a dark band at the top of each block that was deposited continuously without pause. The superimposed hardness profile shows that the dark bands are approximately 100 HV harder than the intermediate four-layer blocks. Both the dark contrast (further illustrated in Extended Data Fig. 1) and the increased hardness result from a precipitation reaction discussed in detail in the next section. These dark bands, on a millimetre–centimetre length scale, represent the coarsest constituent of the hierarchical microstructure of our Damascus-steel sketched in Fig. 1c.

Microstructure analysis

Figure 2 shows a microstructure typical of LAM-produced maraging steels, consisting of a Ni-martensitic matrix with retained austenite occurring in the interdendritic regions. Austenite is stabilized there because the interdendritic regions are enriched in solutes[17,21,22]. Electron backscatter diffraction (EBSD) showed that both the hard bands and the softer regions have a similar austenite fraction and martensite morphology (Fig. 2a). Elemental mapping revealed inhomogeneities in the Ti distribution on two different length scales (Fig. 2b, c). (1) Incomplete mixing of the pre-alloyed Fe20Ni (wt%) powder with elemental Ti powder during fluid flow in the melt pool (Marangoni convection) leads to Ti-enriched regions that are a few hundred micrometres in size. These mixing inhomogeneities do not have an influence on the overall phase fractions. (2) Microsegregation of Ti to the interdendritic regions during solidification leads to micrometre-sized regions enriched in Ti. Figure 2b shows that there are no discernible differences in the distribution or concentration of alloying elements between the hard regions and the soft regions.

Figure 2c illustrates the role of Ti and Ni microsegregation in stabilizing the austenite. The electron micrograph with the overlaid EBSD map shows that the smooth, darker-appearing areas are austenite. Martensite appears brighter because of the rougher surface emitting more secondary electrons. The elemental mapping indicates that the austenite in the interdendritic regions is enriched in Ti and Ni (see Extended Data Fig. 2 for more details of the microstructure characterization at that length scale). This is counterintuitive because Ti is usually classified as a ferrite-stabilizing element in steels. However, we calculated the driving force for martensite formation using Calculation of Phase Diagrams (CALPHAD) simulations, which showed that Ti enrichment lowers the Gibbs energy difference between the austenite and martensite (Extended Data Fig. 3). In this alloy, Ti hence acts as an austenite stabilizer. These dendritic and interdendritic regions resulting from the rapid cooling during DED represent the intermediate constituent of the hierarchical microstructure illustrated in Fig. 1c.

Figure 3a, b shows the fabricated material and a 5-nm-thick slice through an atom probe tomography (APT) reconstruction from analyses of the austenite and martensite in the soft region. Only Ti atoms are shown and they appear randomly distributed in both phases. In

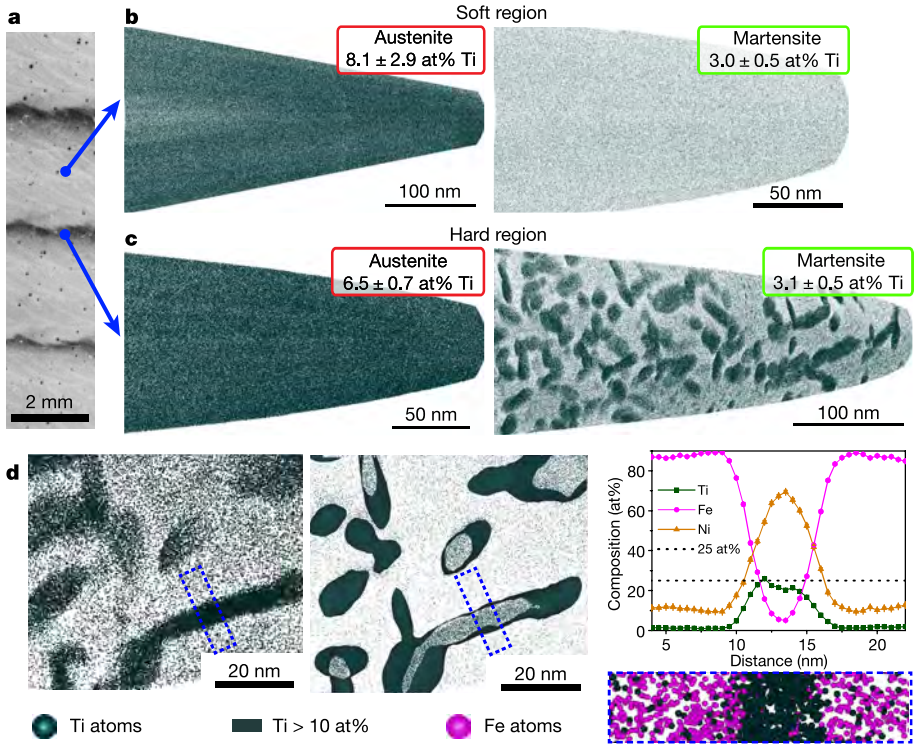

Fig. 3 | APT analysis of martensite and austenite in the soft region and hard region. a, An optical micrograph indicating the positions at which the APT analysis was performed. **b**, **c**, Ti atom maps of a 5-nm-thick slice through the reconstructed volume are shown for the soft region (**b**) and for the hard region (**c**). The left maps shows APT reconstructions from austenite and the right maps show those from martensite. Only the martensite phase forms precipitates upon IHT and only in the hard region. In the soft region, both phases are free of precipitates. **d**, A magnified view of the precipitates by means of Ti atom maps (left) and isocomposition surfaces encompassing regions containing more than 10 at% Ti in dark green (middle). The precipitate is the η-phase $(Ni,Fe)_3Ti$, as can be seen from the one-dimensional composition profile (right) across a precipitate along the dashed blue rectangle. The dashed blue rectangle below the graph shows a magnified view of the rectangles to the left depicting both Fe and Ti atoms as pink and dark green spheres, respectively.

the hard region, however, a high density of precipitates appears in the martensite (Fig. 3c). In this region, two successive phase transformations have occurred: first, an austenite-to-martensite transformation, and second, precipitation inside the martensite. Precipitation occurs only in martensite as the solubility of the alloying elements is higher in austenite. Extended Data Fig. 4 and Supplementary Videos 1 and 2 further illustrate the complex network of precipitates found in this martensite. Averaging over multiple APT datasets, the precipitate volume fraction was determined as 3.50 ± 0.51%.

Precipitates in the Ti atom map in Fig. 3d are highlighted by a set of isocomposition surfaces encompassing regions containing more than 10 at% Ti (dark green). The composition profile across a single plate-shaped precipitate shows that the composition is compatible with η-type Ni_3Ti (for further compositional analysis, see Extended Data Fig. 5). These η-phase precipitates represent the intended precipitate phase selected in the design of our Damascus-like steel. They are the smallest microstructure constituent (Fig. 1c).

Thermal history

Whether η-phase precipitation occurs or not (that is, dark band versus bright region in between) is dictated by the thermal history of the sample during DED: martensite forms only if the temperature drops below the martensite start temperature M_s, and the subsequent cyclic re-heating of the IHT can trigger precipitation (Fig. 4a). The expected phases in this steel appear in the phase diagram isopleth in Extended Data Fig. 6. Figure 4b shows experimental time–temperature profiles from the top surface acquired with a pyrometer during DED using identical process parameters but different pause times after each fourth layer. Without pause time (red solid line), the temperature increases continuously and does not allow the austenite formed upon solidification to transform to martensite. In this case, martensite forms only during the final cool-down after DED, and with no further IHT, no hard bands form (Fig. 4c). In contrast, for samples with a pause in laser illumination, the material cools after each block of four layers. The M_s of the DED-produced Fe19Ni5Ti (wt%) was determined to be 195 °C by dilatometry experiments (Extended Data Fig. 7). During the pause, the temperature drops below M_s and the material of the four layers deposited continuously transforms to martensite (first phase transformation). The subsequent temperature spikes of the IHT trigger η-phase precipitation (second phase transformation). The resulting dark, precipitate-hardened regions appear dark in the optical micrographs in Fig. 4c.

The crucial parameter determining whether precipitation is triggered by the IHT is the temperature drop during the pause (that is, valleys in Fig. 4b). For the sample built with a 30-s pause, the temperature still gradually increases over time, that is, with increasing build height. During the last pause, the temperature only drops to around 180 °C, that is, barely below M_s (orange arrow in Fig. 4b). Only a small fraction of the austenite likely transformed into martensite, and no dark region is discernible for this last pause (that is, the topmost dark region is 'missing', see orange arrow in Fig. 4c). For a sample built with 90-s pauses (shown in Extended Data Fig. 8), the temperature drops below M_s at each pause. However, there is still a slight overall increase in temperature during the build time, causing higher temperature spikes during IHT, which becomes more effective and triggers precipitation to a greater depth into the block of four layers that transformed to martensite during the pause (leading to the broader dark regions towards the top of this sample). For pauses of 180 s (Fig. 4b), the sample cools

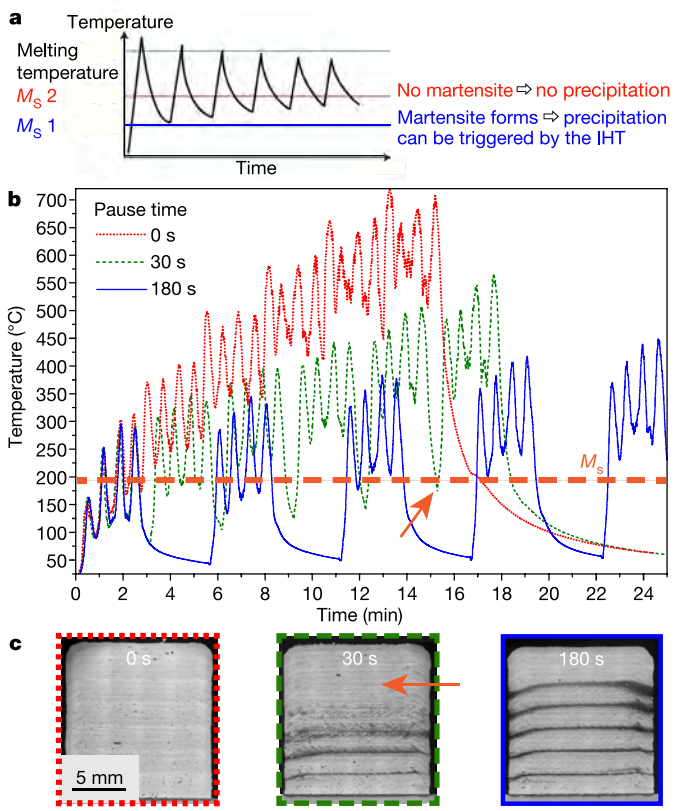

Fig. 4 | The effect of the thermal history. a, A schematic of the IHT. Only if the temperature has dropped below M_s can precipitation be triggered upon the IHT in the martensite phase. **b**, Experimental time–temperature profiles acquired with a pyrometer on the surface of the sample during the DED build at different pause times after each fourth layer. It becomes apparent that without pauses, the temperature increases during the entire fabrication and only drops notably when a pause time is introduced. The dashed orange line corresponds to M_s. The orange arrow points at a temperature drop that barely drops below M_s. **c**, Optical micrographs of the samples built with the corresponding pause times.

to room temperature during each pause. The spikes in temperature during the IHT have a similar height from the bottom to the top of the sample, which results in narrow, dark, precipitation-hardened bands with a constant thickness of a few hundred micrometres.

Mechanical properties

To probe the tensile properties of the digitally engineered Damascus-like microstructures, we prepared a sample deliberately without any pause, which is devoid of precipitates, and a sample with a pause time of 90 s after each layer. This latter Damascus-type steel has a layered structure featuring dark bands at each DED layer. As a pause was introduced after each layer instead of after each fourth layer as in the previous samples, the pause time was shorter. Tensile curves in Fig. 5 show a substantial increase in yield strength and ultimate tensile strength of approximately 200 MPa. Further results, including outliers, are shown in Extended Data Fig. 9a. Interestingly, the precipitation-hardened, layered sample shows not only an increased strength but also an increased elongation at fracture. The simultaneous increase in strength and ductility presumably stems from the Damascus-like, layered microstructure. Further tensile tests in the build direction, reflecting the mechanical anisotropy of the material, are shown in Extended Data Fig. 9b. Impact toughness can be found in Extended Data Fig. 10.

Considering the simplicity of the ternary Fe19Ni5Ti (wt%) alloy, the ultimate tensile strength of greater than 1,300 MPa paired with >10% elongation compares well to complex conventional 18-Ni300 (1.2709) maraging steels produced by LAM: they reach around 1,000–1,200 MPa ultimate tensile strength with 8–12% elongation in the as-produced state and 1,800–2,100 MPa with 1.5–5.0% elongation in the aged condition[17,24,25]. Conventionally produced 18-Ni300 reaches similar tensile strengths of around 2,000 MPa but has a slightly higher elongation at fracture of around 10%.

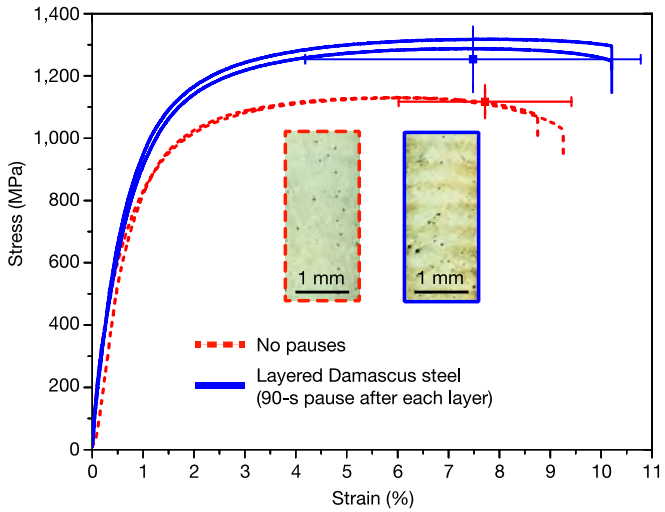

Fig. 5 | Tensile tests of two Fe19Ni5Ti (wt%) steel samples. One Damascus-like sample containing precipitation-hardened bands and a sample containing no precipitates. Only the sample with the pause time (90 s in this case) can cool below M_s during the process and therefore contains martensite hardened by $(Fe,Ni)_3Ti$ precipitates. Two representative curves are shown for each condition together with the average value for maximum tensile strength and elongation at fracture. The insets show the corresponding optical micrographs.

Conclusions

We have shown here that hierarchically structured Damascus-like metallic composites can be directly synthesized in situ by additive manufacturing using digital control of the IHT sequences associated with the layer-wise fabrication technique. More specifically, we used a nanostructured martensitic (maraging) steel. Using controlled pausing between alternating layers, we built a composite microstructure with excellent mechanical properties (1,300 MPa and 10% elongation). Its structure consists of mesoscopic soft regions, that is, devoid of nanoprecipitates, and hard regions containing a high volume fraction of nanoscale precipitates. These precipitates form over the course of the IHT following the martensitic transformation, which is itself triggered during the cooling offered by the pause. This achievement was enabled by the design of an Fe19Ni5Ti (wt%) alloy specifically for LAM that allows us to tune the start temperature of the martensite transformation and hence the precipitation during the process.

Here we have chosen to vary the pause time between layers because its influence on the temperature is very intuitive and measurable. The local sample temperature can, however, be controlled by a variety of process parameters such as laser power, scan speed, external heating and cooling, and so on, or a combination thereof. This makes the approach presented here applicable to a wide range of additive manufacturing processes. Furthermore, in situ hardening exploiting the IHT can be extended to other precipitation-hardening alloys. The opportunity to locally tailor microstructures and mechanical properties provides new possibilities for manufacturing. As an example, one could manufacture tools that are soft and tough on the inside and only the outer skin is precipitation hardened without the need to apply a coating or a case-hardening treatment.

Online content

Any methods, additional references, Nature Research reporting summaries, source data, extended data, supplementary information, acknowledgements, peer review information; details of author contributions and competing interests; and statements of data and code availability are available at https://doi.org/10.1038/s41586-020-2409-3.

1. Herzog, D., Seyda, V., Wycisk, E. & Emmelmann, C. Additive manufacturing of metals. *Acta Mater*. **117**, 371–392 (2016).
2. Sames, W. J., List, F. A., Pannala, S., Dehoff, R. R. & Babu, S. S. The metallurgy and processing science of metal additive manufacturing. *Int. Mater. Rev*. **61**, 315–360 (2016).
3. Gu, D. D., Meiners, W., Wissenbach, K. & Poprawe, R. Laser additive manufacturing of metallic components: materials, processes and mechanisms. *Int. Mater. Rev*. **57**, 133–164 (2012).
4. Xu, W., Lui, E. W., Pateras, A., Qian, M. & Brandt, M. In situ tailoring microstructure in additively manufactured Ti-6Al-4V for superior mechanical performance. *Acta Mater*. **125**, 390–400 (2017).
5. Haubrich, J. et al. The role of lattice defects, element partitioning and intrinsic heat effects on the microstructure in selective laser melted Ti-6Al-4V. *Acta Mater*. **167**, 136–148 (2019).
6. Krakhmalev, P., Yadroitsava, I., Fredriksson, G. & Yadroitsev, I. In situ heat treatment in selective laser melted martensitic AISI 420 stainless steels. *Mater. Des*. **87**, 380–385 (2015).
7. Mazumder, J., Choi, J., Nagarathnam, K., Koch, J. & Hetzner, D. The direct metal deposition of H13 tool steel for 3-D components. *JOM* **49**, 55–60 (1997).
8. Cottam, R., Wang, J. & Luzin, V. Characterization of microstructure and residual stress in a 3D H13 tool steel component produced by additive manufacturing. *J. Mater. Res*. **29**, 1978–1986 (2014).
9. Kürnsteiner, P. et al. Massive nanoprecipitation in an Fe-19Ni-*x*Al maraging steel triggered by the intrinsic heat treatment during laser metal deposition. *Acta Mater*. **129**, 52–60 (2017).
10. Costa, L., Vilar, R., Reti, T. & Deus, A. M. Rapid tooling by laser powder deposition: process simulation using finite element analysis. *Acta Mater*. **53**, 3987–3999 (2005).
11. Mintách, R., Nový, F., Bokůvka, O. & Chalupová, M. Impact strength and failure analysis of welded Damascus steel. *Mater. Eng*. **19**, 22–28 (2012).
12. Peterson, D. T., Baker, H. H. & Verhoeven, J. D. Damascus steel, characterization of one Damascus steel sword. *Mater. Charact*. **24**, 355–374 (1990).
13. Verhoeven, J. D. Genuine Damascus steel: a type of banded microstructure in hypereutectoid steels. *Steel Res*. **73**, 356–365 (2002).
14. Černý, M., Filípek, J., Mazal, P. & Dostál, P. Basic mechanical properties of layered steels. *Acta Univ. Agric. Silvic. Mendel. Brun*. **61**, 25–38 (2013).
15. Zheng, B., Zhou, Y., Smugeresky, J. E., Schoenung, J. M. & Lavernia, E. J. Thermal behavior and microstructural evolution during laser deposition with laser-engineered net shaping: Part I. Numerical calculations. *Metall. Mater. Trans. A* **39**, 2228–2236 (2008).
16. Kürnsteiner, P. et al. Control of thermally stable core–shell nano-precipitates in additively manufactured Al-Sc-Zr alloys. *Addit. Manuf*. **32**, 100910 (2020).
17. Bajaj, P. et al. Steels in additive manufacturing: a review of their microstructure and properties. *Mater. Sci. Eng. A* **722**, 138633 (2020).
18. Sha, W., Cerezo, A. & Smith, G. D. W. Phase chemistry and precipitation reactions in maraging steels: Part IV. Discussion and conclusions. *Metall. Trans. A* **24**, 1251–1256 (1993).
19. Pereloma, E. V., Shekhter, A., Miller, M. K. & Ringer, S. P. Ageing behaviour of an Fe-20Ni-1.8Mn-1.6Ti-0.59Al (wt%) maraging alloy: clustering, precipitation and hardening. *Acta Mater*. **52**, 5589–5602 (2004).
20. Bodziak, S. et al. Precipitation in 300 grade maraging steel built by selective laser melting: aging at 510 °C for 2 h. *Mater. Charact*. **151**, 73–83 (2019).
21. Jägle, E. A. et al. Comparison of maraging steel micro- and nanostructure produced conventionally and by laser additive manufacturing. *Materials* **10**, 8 (2017).
22. Tan, C. et al. Microstructural evolution, nanoprecipitation behavior and mechanical properties of selective laser melted high-performance grade 300 maraging steel. *Mater. Des*. **134**, 23–34 (2017).
23. Pereloma, E. V., Stohr, R. A., Miller, M. K. & Ringer, S. P. Observation of precipitation evolution in Fe-Ni-Mn-Ti-Al maraging steel by atom probe tomography. *Metall. Mater. Trans*. **40**, 3069–3075 (2009).
24. Casati, R., Lemke, J., Tuissi, A. & Vedani, M. Aging behaviour and mechanical performance of 18-Ni 300 steel processed by selective laser melting. *Metals* **6**, 218 (2016).
25. Hermann Becker, T. & Dimitrov, D. The achievable mechanical properties of SLM produced maraging Steel 300 components. *Rapid Prototyp. J*. **22**, 487–494 (2016).

Methods

Laser additive manufacturing

Pre-alloyed Fe20Ni (wt%) powder mixed with commercially pure Ti powder to obtain Fe19Ni5Ti (wt%) was used to manufacture samples for this study by DED. Both powders were gas atomized under argon. The Fe20Ni powder was purchased from Nanoval and the pure Ti powder was purchased from TLS Technik. Both powders had a particle fraction of 45–90 µm.

For DED, we used a five-axis handling system equipped with a fibre-coupled diode laser system LDM 3000-60 (Laserline) with a wavelength of 976 nm and a beam parameter product of 60 mm mrad. The final beam diameter of 1.8 mm was obtained through a collimation lens (focal length f_c = 65 mm) and a focusing lens (f_f = 195 mm). A disk-based powder feeding system Sulzer Metco Twin 10C (OC Oerlikon) was used to feed the dry mixed Fe20Ni powder and Ti powder. Argon was used as both the shielding gas and the carrier gas. We applied a bidirectional scan strategy, depositing 20 single tracks with a constant track offset of 0.8 mm (in-plane) with a deposition speed of 600 mm min^{-1} and a laser power of 550 W. The optical setup was moved after completion of each layer by a constant height offset of 0.62 mm (plane to plane) in the building direction. Samples were built on 1.2365 (AISI H10) steel substrate plates. While the aforementioned parameters were kept constant among all samples in this study, we exploited the flexibility of the computer-controlled process to vary a single process parameter, namely, the interlayer pause time. The main sample of this study on which we carried out an in-depth microstructure analysis was produced with 120-s pause time after each fourth layer. This means that after depositing a 'block' of four layers with continuous laser illumination, the process was interrupted for 120 s, during which no heat was imposed by the laser. To measure the cooling during this pause time, samples with different pause times between 0 and 180 s after each fourth layer were produced and the temperature was monitored in situ with a pyrometer. The layered, Damascus-type steel sample with a pause time of 90 s after each layer was selected for in-depth mechanical property characterization, by both tensile and impact testing. The mechanical properties were compared with a sample built without any pause. The pause time of 90 s was chosen to assure cooling of the material below M_s after each layer was deposited, to trigger in situ precipitation with the IHT exerted by the subsequent build layer. Compared with the sample with a pause only after each fourth layer, this sample required a shorter pause time to achieve sufficient cooling because of the more frequent pauses. It is noted that the interlayer pause time is a typical LAM process parameter that is set digitally together with all the other parameters and input into the DED machine.

A LaserSight (Optris) infrared pyrometer was used to acquire the time–temperature profiles during the DED build. After each layer, the pyrometer was moved upwards the same distance as the DED layer height.

Analytical methods

Scanning electron microscopy (SEM) to obtain electron micrographs as well energy dispersive X-ray spectroscopy (EDS) to obtain element mappings was performed in a Zeiss Merlin (Carl Zeiss SMT) featuring a Gemini 2-type field emission gun (FEG) electron column. For EDS, a Brucker XFlash 6/30 silicon drift detector featuring a 30-mm^2 detector area was used. EBSD was performed on a Zeiss 1540XB cross-beam SEM-focused ion beam (FIB) setup featuring a Gemini 1 FEG electron column. EBSD was performed using an EDAX Hikari camera. The TSL OIM Analysis software (version 7) was used for EBSD data analysis. An acceleration voltage of 15 kV was used for EDS and EBSD. Samples for SEM-based techniques were prepared using standard metallographic techniques. For light optical microscopy (LOM) and secondary electron (SE) imaging in the SEM, the samples were etched using 5 vol% nital (HNO_3 in ethanol).

APT samples were prepared by the standard lift-out process[26] in a Thermo Fisher Scientific Helios NanoLab 600i dual-beam FIB/SEM device. We sharpened the APT tips by annular milling at 30 kV followed by a low kilovolt milling at 5 kV for 1 min. APT tips from the middle of the precipitation-hardened band as well as from the softer region in between the precipitation-hardened bands were prepared.

APT experiments were performed in a Cameca LEAP 5000 XR and a 5000 XS in laser-pulsing mode. A pulse frequency between 125 and 333 kHz on the 5000 XR and between 250 and 625 kHz on the 5000 XS, a pulse energy between 40 and 75 pJ, and a temperature between 40 and 60 K were used. The detection rate was set between 1 and 4%. The commercial Integrated Visualization and Analysis Software (IVAS, version 3.8.2) was used to reconstruct the tip volume. Voxel-based analysis was performed with a grid spacing of 1 nm and a delocalization of 2 nm.

When analysing the η-phase $(Ni,Fe)_3Ti$ precipitates, one has to take into account the local magnification artefacts due to the differences in evaporation field between the matrix and the precipitate[27–29]. The field of evaporation of the η-phase precipitate is much higher than that of the matrix, which leads to an 'outwards projection' of the ion trajectories of the precipitate phase. Consequently, this leads to an artificially increased apparent volume as well as a lowered apparent density of the precipitate in the APT reconstruction. Simply extracting the volume enclosed by the isocomposition surfaces to calculate precipitate volume would lead to a substantial overestimation of the volume fraction. Therefore, we extracted the number of Ti atoms enclosed by the isocomposition surfaces $N_{Ti,prec}$ and calculated the volume fraction by dividing the number of atoms inside the precipitates (that is, $4 \times N_{Ti,prec}$) by the number of atoms in the entire reconstruction. In addition, we corrected the volume fraction for the slightly larger density of Ni_3Ti compared with Fe.

We acquired multiple datasets from multiple APT tips for each phase in both regions (that is, martensite as well as austenite in the precipitation-hardened bands as well as in the soft regions). None of the measurements of austenite and ferrite in the soft region as well as austenite in the hard region showed any indications of notable clustering of Ti and/or Ni. For the calculation of the precipitate volume fraction in the martensitic phase in the hard regions, we averaged over four individual APT measurements sampling over 24 million nm^3 in total (equivalent to detecting over 1.3 billion ions).

From correlative EBSD and EDS measurements, it is known that the interdendritic regions enriched in Ni and Ti represent the austenite phase, while martensite is depleted in both elements and represents the dendritic regions. Using this knowledge, it is possible to relate each APT reconstruction to either austenite or martensite via the Ti and Ni content in the APT measurements. In the soft regions, the mean Ni and Ti content in the austenite was 21.5 ± 2.7 at% and 8.1 ± 2.9 at% and in the martensite was 16.7 ± 0.3 at% and 3.0 ± 0.5 at%. In the hard regions, the mean Ni and Ti content in the austenite was 19.3 ± 0.1 at% and 6.5 ± 0.7 at% and in the martensite 16.3 ± 0.2 at% and 3.1 ± 0.5 at%.

Vickers hardness measurements along the build direction of the sample were performed using a LECO M-400-G (LECO Instrumente).

Thermo-Calc software (version 2016) together with the TCFE7 database was used to calculate the Gibbs energies of the face-centred cubic (fcc) and body-centred cubic (bcc) phases as a function of the Ti content.

For tensile testing, a Zwick Z100 equipped with a laserXtens 2 HP/TZ laser extensometer was used. Tests were performed at room temperature at a strain rate of 10^{-3} mm min^{-1} on dog-bone-shaped samples with a gauge length of 25 mm, a thickness of 1 mm, a gauge width of 5 mm and a total length of 45 mm. These specimens were machined with the gauge length parallel to the laser scan direction. Further, smaller, test specimens (4-mm gauge length, 2-mm gauge width and 0.35-mm gauge thickness) were machined with the gauge length parallel to the build direction (that is, perpendicular to the layered structure) and the gauge width parallel to the laser scan direction. These samples were tested in

a Kammrath and Weiss tensile testing stage at room temperature and at a strain rate of 2 μm s^{-1}. The strain was measured by digital image correlation using the Aramis software (GOM). The results are shown in the Extended Data Fig. 9b.

Dilatometer experiments were carried out in a Bähr Thermoanalyse DIL805A/D dilatometer using hollow cylindrical specimens with a height of 1 cm, an outer diameter of 4.5 mm and an inner diameter of 2 mm at a heating rate of 600 °C min^{-1} and a cooling rate of 160 °C min^{-1}.

Supplementary discussion of the alloy design concept

LAM is currently mostly applied to conventional alloys, with compositions not optimized for the specific conditions encountered during the fabrication. This can lead to severe problems regarding processability and furthermore leaves aside opportunities for alloy design and tailored microstructures. Here we designed a new steel optimized and tailor-made for LAM exploiting two specific conditions of LAM, namely rapid quenching and cyclic re-heating (the so-called IHT). We considered three key requirements that the steel needed to fulfil:

(1) A martensitic microstructure after fabrication.

(2) An M_s value that lies in a control window that is readily accessible to the digital control exerted during the DED process

(3) A kinetic window to respond in the desired way and quickly to the IHT with a substantial precipitation reaction.

All three factors drove the design of the steel, that is, the selection of the composition. The exact precipitation kinetics (especially during the very nonlinear heat treatment of the IHT) as well as the microstructure after rapid quenching during LAM turned out to be challenging to predict. Therefore, we used a rapid alloy prototyping approach, whereby we built a compositionally graded sample using DED. This preliminary fabrication allowed us to efficiently screen the microstructure and the response to the IHT as a function of the alloy composition. For an Fe–Ni–Al steel, this approach has been outlined and explained in more detail in our previous study[9].

Data availability

The authors declare that the data supporting the findings of this study are available within the paper and its supplementary information and extended data files. Raw data are available from the corresponding author upon reasonable request.

26. Larson, D. J., Prosa, T. J., Ulfig, R. M., Geiser, B. P. & Kelly, T. F. *Local Electrode Atom Probe Tomography: A User's Guide* (Springer, 2013).
27. Vurpillot, F., Bostel, A. & Blavette, D. Trajectory overlaps and local magnification in three-dimensional atom probe. *Appl. Phys. Lett.* **76**, 3127–3129 (2000).
28. Lefebvre, W. et al. 3DAP measurements of Al content in different types of precipitates in aluminium alloys. *Surf. Interface Anal.* **39**, 206–212 (2007).
29. Marquis, E. A. & Vurpillot, F. Chromatic aberrations in the field evaporation behavior of small precipitates. *Microsc. Microanal.* **14**, 561–570 (2008).
30. Hellman, O. C., Vandenbroucke, J. A., Rüsing, J., Isheim, D. & Seidman, D. N. Analysis of three-dimensional atom-probe data by the proximity histogram. *Microsc. Microanal.* **6**, 437–444 (2000).
31. Casati, R., Lemke, J. & Vedani, M. Microstructure and fracture behavior of 316L austenitic stainless steel produced by selective laser melting. *J. Mater. Sci. Technol.* **32**, 738–744 (2016).
32. Kim, H., Liu, Z., Cong, W. & Zhang, H. C. Tensile fracture behavior and failure mechanism of additively-manufactured AISI 4140 low alloy steel by laser engineered net shaping. *Materials* **10**, 1283 (2017).
33. Kasper, R. & Faul, H. Charpy-V subsize specimens: measurements of steel impact properties. *Materialpruefung* **43**, 18–21 (2001).
34. Lucas, G. E., Odette, G. R., Sheckherd, J. W. & Krishnadev, M. R. Recent progress in subsized Charpy impact specimen testing for fusion reactor materials development. *Fusion Technol.* **10**, 728–733 (1986).
35. Schill, R., Forget, P. & Sainte Catherine, C. Correlation between Charpy-V and sub-size Charpy tests results for an un-irradiated low alloy RPV ferritic steel. In *Thirteenth European Conference on Fracture* (Elsevier, 2000).
36. Kempen, K., Yasa, E., Thijs, L., Kruth, J. P. & Van Humbeeck, J. Microstructure and mechanical properties of selective laser melted 18Ni-300 steel. *Phys. Proc.* **12**, 255–263 (2011).

Acknowledgements We are grateful to U. Tezins and A. Sturm for their support to the FIB and APT facilities at MPIE, to H. Faul and A. Jansen for their help with tensile tests, and to M. Adamek for his help with dilatometer experiments. A. Kwiatkowski da Silva and P. Bajaj are acknowledged for their input and discussions regarding thermodynamics and additive manufacturing respectively. We thank C. Brunner-Schwer for his support in conducting the DED experiments.

Author contributions P.K. performed the microstructure analysis and corresponding data analysis including EDS, EBSD, FIB and APT and the analysis of dilatometer experiments and tensile tests. M.B.W. produced all samples used in this study by DED and acquired the experimental thermal profiles as well as the optical micrographs. E.A.J., A.W., B.G. and D.R. designed the study and acquired funding. P.K. wrote the initial draft. All authors contributed to reviewing and editing the manuscript and discussing and interpreting all the results.

Competing interests The authors declare no competing interests.

Additional information
Supplementary information is available for this paper at https://doi.org/10.1038/s41586-020-2409-3.
Correspondence and requests for materials should be addressed to P.K.
Peer review information *Nature* thanks Claire Davis and the other, anonymous, reviewer(s) for their contribution to the peer review of this work.
Reprints and permissions information is available at http://www.nature.com/reprints.

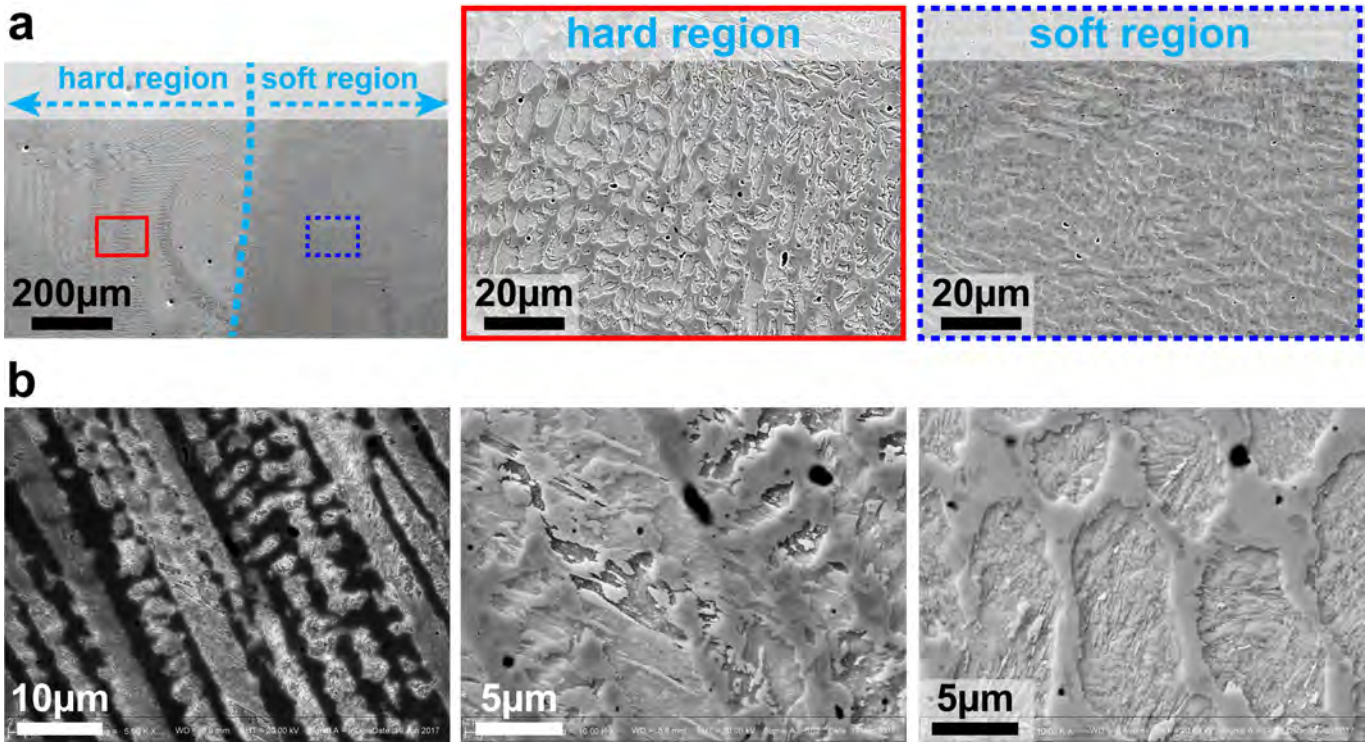

Extended Data Fig. 1 | Electron micrographs of the soft and hard regions. In the SE micrographs, the hard region appears bright due to the rougher surface emitting more SEs, while the soft region appears darker due to the smooth surface (that is, opposite of how these two regions appear in optical micrographs). **a**, The interface between the soft and hard regions as well as a zoom to both regions. It is apparent that in the hard region there are two distinct phases: one with a rough surface, which is the martensite with $(Ni,Fe)_3Ti$ precipitates, and one with a smooth surface, which is austenite (and does not contain any precipitates). In the soft region, both austenite and martensite have a smooth surface as the martensite does not contain any precipitates in the soft regions. **b**, Further examples of the rough surfaces in hard regions at higher magnifications. The sample was slightly etched with 5 vol% nital for 10 s at room temperature.

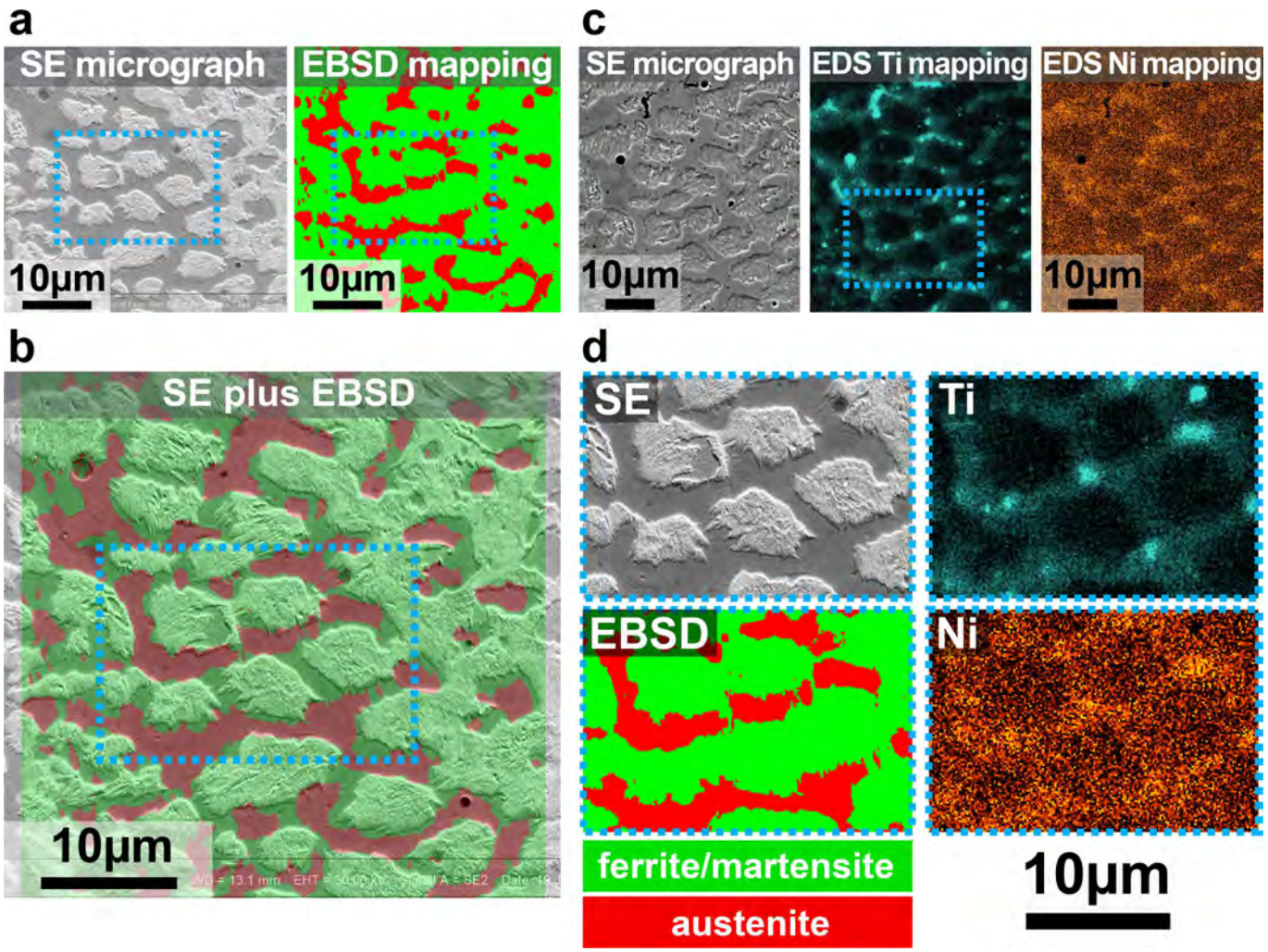

Extended Data Fig. 2 | Microstructure characterization. High-resolution EBSD together with correlative EDS elemental mapping of a location within a hard region, showing that the austenite is enriched in Ti and Ni. **a**, SE micrograph (left) and EBSD mapping (right) of the same location. **b**, Overlapping the SE micrograph and the EBSD phase map from **a** show that austenite has a smooth surface and appears darker than martensite with a rough surface. **c**, The EDS element mapping shows that the smooth regions (that is, austenite) are enriched in Ti and Ni. These regions represent the interdendritic regions. **d**, EDS and EBSD are brought together: the area shown in **d** is marked by light blue dashed boxes in **a**–**c**. It becomes apparent that austenite has a smooth surface and is enriched in Ti and Ni, whereas martensite has a rough surface and is depleted in Ti and Ni.

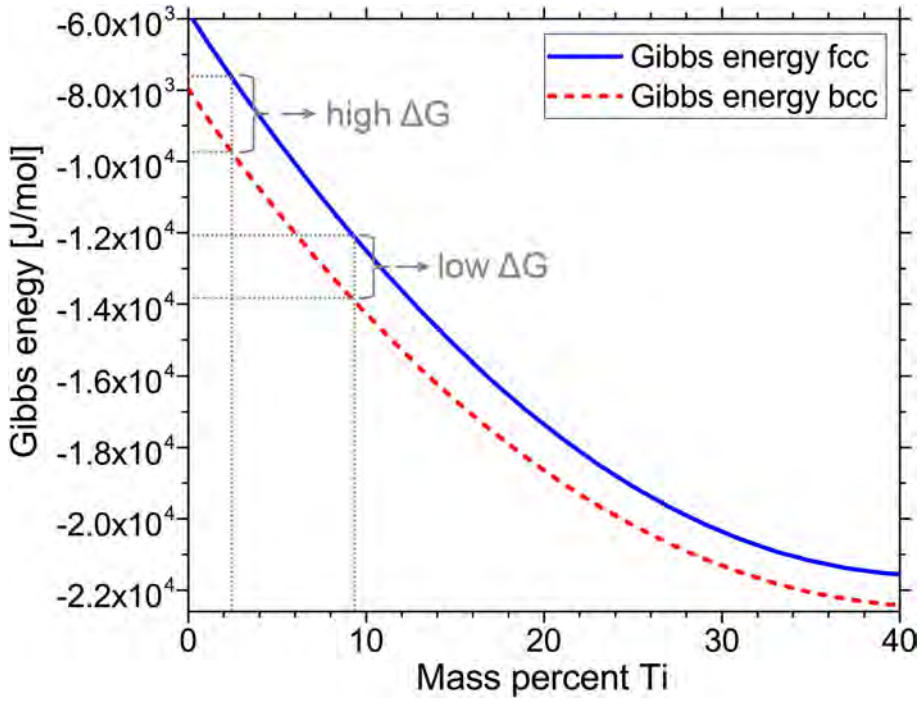

Extended Data Fig. 3 | Thermodynamic calculation of the driving force for martensite formation. The Gibbs free energies of single-phase bcc and fcc Fe–Ni–Ti at room temperature for a variable Ti content and a fixed Ni content of 19 wt%. It is apparent that there is a higher energy difference between the fcc and bcc structures (that is, a higher driving force for martensite formation) at lower Ti contents than at higher Ti contents. The two Ti compositions highlighted in the graph are 2.3 wt% Ti and 8.6 wt% Ti, which are typical compositions for the martensite/dendritic region and the austenite/interdendritic region, respectively, and for which the driving force for martensite formation is −2,100 J mol^{-1} and −1,780 J mol^{-1}, respectively.

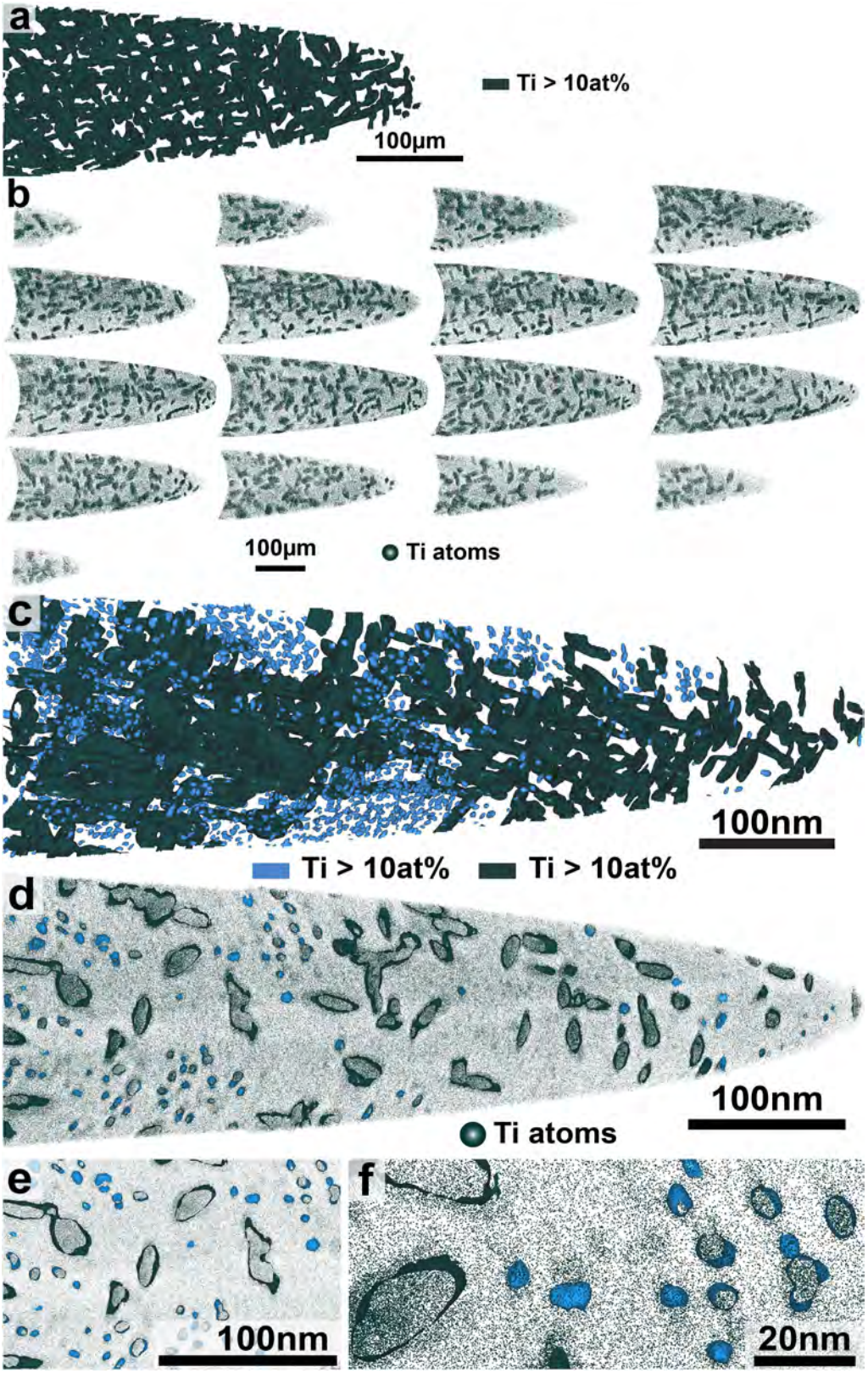

Extended Data Fig. 4 | Serial sections through an APT reconstruction. **a**, The $(Ni,Fe)_3Ti$ precipitates are marked by a 10 at% Ti isocomposition surface in the APT reconstruction. **b**, Consecutive slices through the same dataset from one side of the tip to the other. Each slice is 10 nm thick and all Ti atoms within this slice are shown. This sequence of images illustrates the complex shape and morphology and three-dimensional arrangement of the network of η-phase $(Ni,Fe)_3Ti$ precipitates created by IHT during the DED process. **c**–**f**, Reconstruction of an APT volume that contains small spherical precipitates a few nanometres in diameter in addition to the plate-shaped interconnected network of precipitates. Both precipitate types are η-phase $(Ni,Fe)_3Ti$ and are marked by means of 10 at% Ti isocomposition surfaces. The plate-shaped network is depicted in dark green and the small spherical precipitates are depicted in light blue. In **c**, the whole dataset is shown, and in **d**–**f**, only a thin slice of 5 nm thickness is shown. In addition to the isocomposition surfaces, Ti atoms are shown in **d**–**f**. Panels **e** and **f** are enlarged sections of the image shown in **c**.

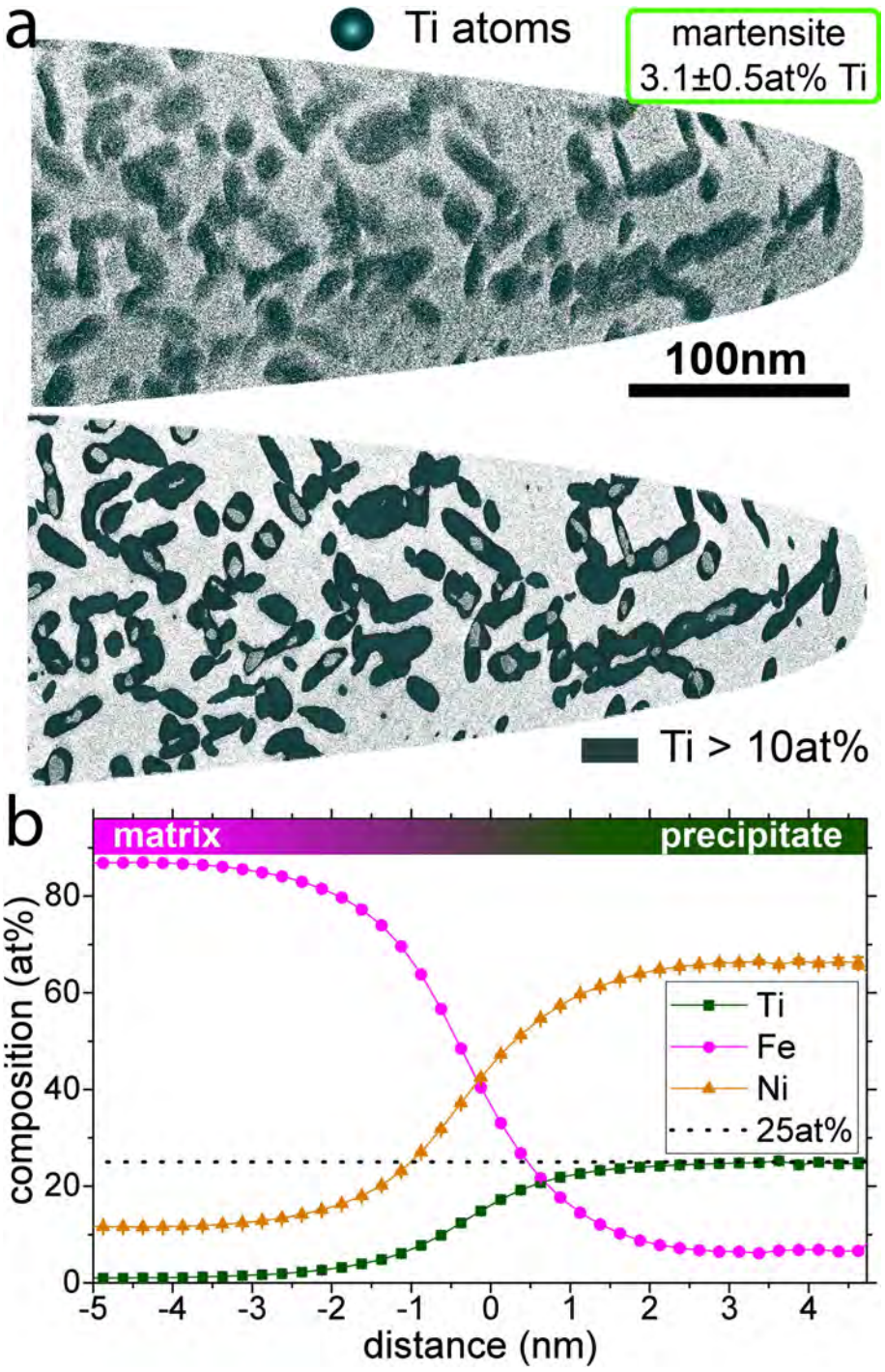

Extended Data Fig. 5 | Composition of the η-phase precipitates. a, A Ti atom map of a 5-nm-thick slice through the reconstructed volume from the martensitic phase in the hard region. The top part shows the atom map only; in the bottom part, precipitates are also highlighted by a set of isocomposition surfaces encompassing regions containing more than 10 at% Ti (dark green). **b**, A proximity histogram, that is, composition profile as a function of the distance to this isocomposition surface[30], calculated for all imaged precipitates in the dataset. The average Ti content fits the expected 25 at% almost perfectly. Fe replaces some of the Ni from the prototype Ni_3Ti phase, rendering it a $(Ni,Fe)_3Ti$ phase with approximately 6–7 at% Fe and 66–67 at% Ni.

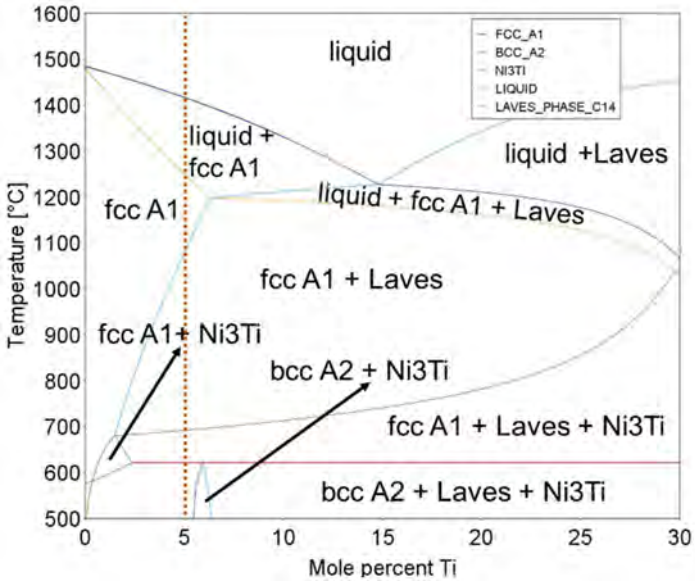

Extended Data Fig. 6 | Pseudobinary phase diagram for the Fe19Ni-*x*Ti (at%) alloy. The phase diagram was calculated using the Thermo-Calc software in conjunction with the TCFE7 database. The dashed line at 5 at% Ti highlights the phases that can be expected for the Fe19Ni5Ti (at%) steel used in this study: liquid, fcc A1 austenite, η-phase Ni_3Ti, Laves phase and bcc A2 ferrite/martensite.

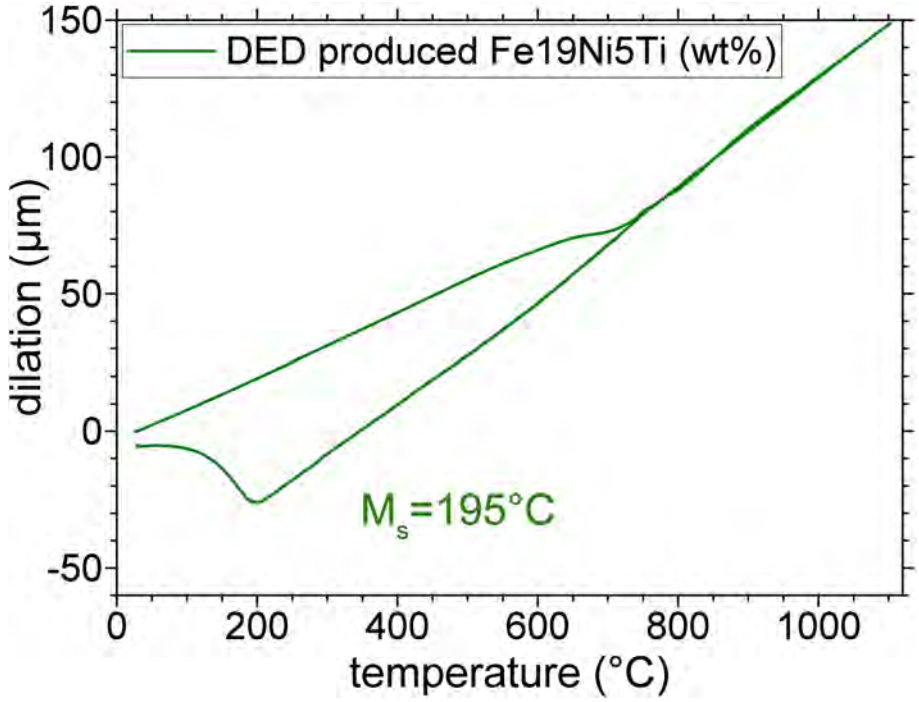

Extended Data Fig. 7 | Determination of M_s. A dilatometer curve acquired on a DED-produced Fe19Ni5Ti (wt%) sample (with no pause) is depicted. The double tangent method was used to determine M_s as 195 °C. Further dilatometer specimen from the same DED sample as well as DED samples with a 90-s pause time were measured. On all measurements, the martensite start temperatures are within 10 °C.

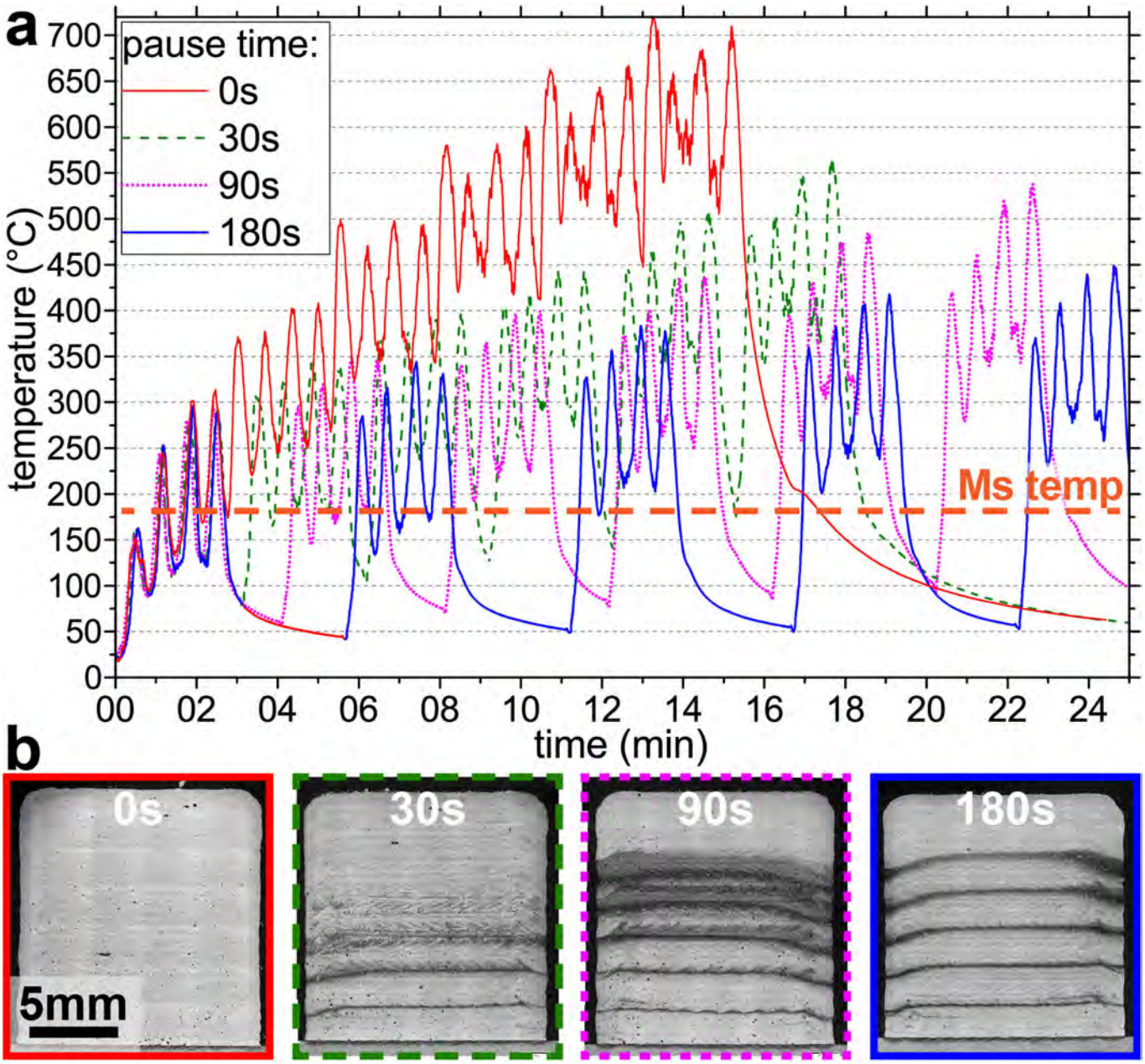

Extended Data Fig. 8 | Experimental time–temperature profiles. **a**, Experimental time–temperature profiles acquired with a pyrometer on the surface of the sample during the DED build at different pause times after each fourth layer. It becomes apparent that without pauses, the temperature increases during the entire fabrication and only drops notably when a pause time is introduced. The dashed orange line corresponds to M_s. **b**, Optical micrographs of the samples built with the corresponding pause times.

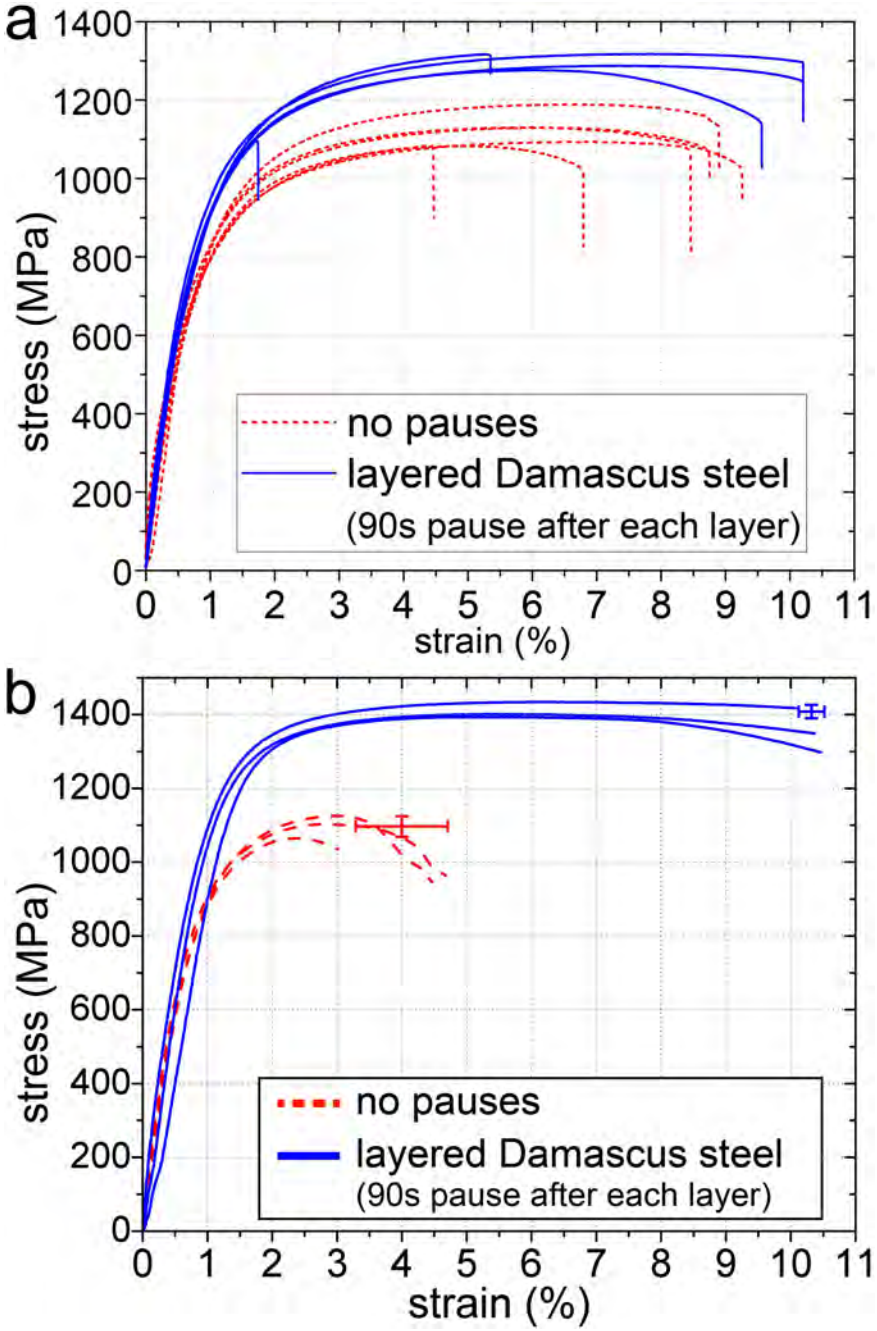

Extended Data Fig. 9 | Tensile curves. a, The testing direction is parallel to the laser scan direction. Tensile tests show a substantial improvement in strength as well as ductility when a pause is introduced in the manufacturing process. The pause allows the material to partially transform to martensite and then allows the IHT to trigger $(Fe,Ni)_3Ti$ precipitates in the martensite. The results show a few tensile specimens that fracture prematurely at low strains, which is due to additive-manufacturing-process-related defects[31,32]. These outliers rather represent the additive manufacturing process and show that there is potential for future process optimization. The specimens containing fewer defects and therefore higher strength and ductility show the actual potential of the newly designed maraging steel. In Fig. 5, we show two representative curves for each condition. For the condition '90-s pause each layer', we omitted the one sample fracturing prematurely at 1.7% strain as well as the samples with the highest strength and lowest strength and show the two curves in between. For the condition 'no pauses', we omitted the two samples fracturing at the lowest strains of 4.5% and 6.7% as well as the samples with the lowest strength and highest strength. **b**, The testing direction is parallel to the build direction. Owing to limitations in the size of the DED-produced samples, we used small tensile specimens with a gauge length of 4 mm, a width of 2 mm and a thickness of 0.35 mm to test the tensile properties along the build direction (that is, perpendicular to the layered structure). The tensile specimens were machined with the gauge width parallel to the laser scan direction. There is a notable increase in strength and ductility due to the layered, Damascus-type structure. However, due to the smaller size, compared with the tensile specimen machined along the laser scan direction, a direct comparison between the two is difficult. Both, the Damascus-type layered steel as well as the one that was produced without pauses in between layers show higher strengths along the build direction than in the laser scan direction. While this could be due to the anisotropy of the material, the smaller tensile specimen geometry might also have a role.

a

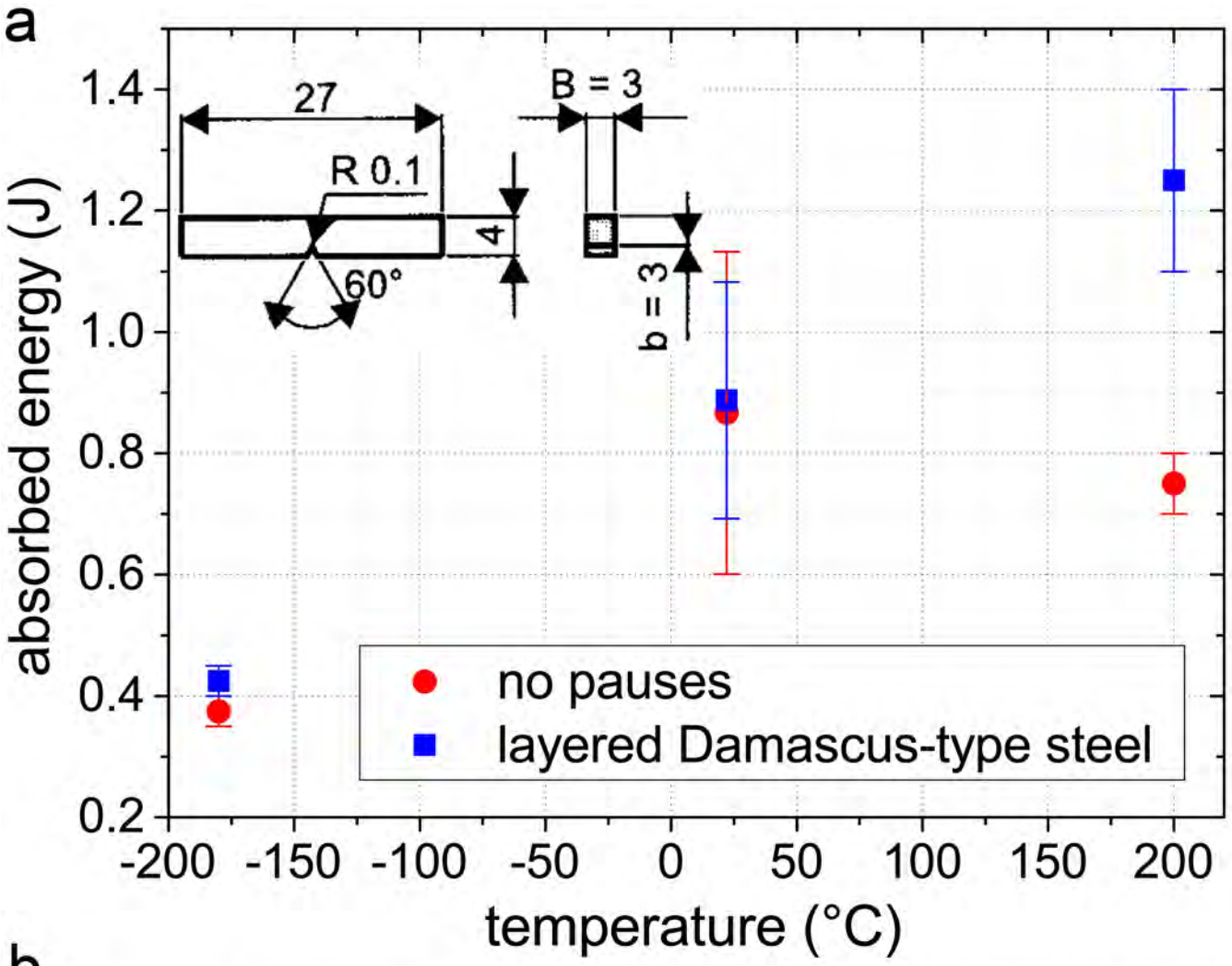

b

	Temperature [°C]	Absorbed energy [J]	Normalized absorbed energy (factor B*b) [J]	Normalized absorbed energy (factor B*b²) [J]
No pause	-180	0.38	3.33	8.89
	22	0.87	7.70	20.54
	200	0.75	6.67	17.78
Damascus-type	-180	0.43	3.78	10.07
	22	0.89	7.89	21.04
	200	1.25	11.11	29.63

Extended Data Fig. 10 | Impact toughness. a, The absorbed energies of subsized V-notch Charpy specimens at three different temperatures of −180 °C, 22 °C and 200 °C. The inset shows the geometry of the used subsized specimens. Charpy specimens were machined along the laser scan direction of the DED sample with the *B* direction normal to the layers and the *b* direction parallel to the layers. The values shown in the graph are an average of three specimens at 22 °C and two specimens at −180 °C and 200 °C. **b**, The values of the absorbed energy in joules in the Charpy V-notch impact testing carried out on subsized specimens shown in the inset in **a**. Two different normalizing factors are used to convert the results of the subsized specimen to standard specimen ($55 \times 10 \times 8\ mm^3$): the fracture area $B \times b$ and the fracture volume $B \times b^2$ (see, for example, refs. [33–35]). It is noted that such normalizing factors are material dependent and there is no literature available on the selection of normalizing factors for additively manufactured maraging steels. The converted values presented in this table should therefore only be regarded as a rough estimate of the impact toughness on standard samples. Nevertheless, the Fe19Ni5Ti (wt%) samples investigated in this study show a high impact toughness compared with 4.9 J (standard V-notch samples) of laser-powder-bed-fusion-produced 18Ni-300 maraging steel in the aged condition (5 h at 480 °C)[36].